Two-Dimensional Flow Boiling Characteristics With Wettability Surface in Microgap Heat Sink and Heat Transfer Prediction Using Artificial Neural Network

Anwarul Karim
School of Engineering and Computer Science,
Washington State University,
Vancouver, WA 98686

Yoon Jo Kim
Intel Corp.,
2501 NE Century Boulevard,
Hillsboro, OR 97124

Jong-Hoon Kim[1]
School of Engineering and Computer Science,
Washington State University,
Vancouver, WA 98686
e-mail: jh.kim@wsu.edu

As technology becomes increasingly miniaturized, thermal management becomes challenging to keep devices away from overheating due to extremely localized heat dissipation. Two-phase cooling or flow boiling in microspaces utilizes the highly efficient thermal energy transport of phase change from liquid to vapor. However, the excessive consumption of liquid-phase by highly localized heat source causes the two-phase flow maldistribution, leading to a significantly reduced heat transfer coefficient, high-pressure loss, and limited flow rate. In this study, flow boiling in a two-dimensional (2D) microgap heat sink with a hydrophilic coating is investigated with bubble morphology, heat transfer, and pressure drop for conventional (nonhydrophilic) and hydrophilic heat sinks. The experiments are carried out on a stainless steel (SS) plate, having a microgap depth of 170 μm using de-ionized (DI) water at room temperature. Two different hydrophilic surfaces (partial and full channel shape) are fabricated on the heated surface to compare the thermal performance with the conventional surface. Vapor films and slugs are flushed quickly on the hydrophilic surfaces, resulting in heat transfer enhancement on the hydrophilic heat sink compared to the conventional heat sink. The channel hydrophilic heat sink shows better cooling performance and pressure stability as it provides a smooth route for the incoming water to cool the hot spot. Moreover, the artificial neural network (ANN) prediction of heat transfer coefficient shows a good agreement with the experimental results as data fit within ±5% average error. [DOI: 10.1115/1.4051602]

Keywords: flow boiling, microgap, hydrophilic, two-phase flow, ANN

1 Introduction

With technological advancement, electronic devices become more compact and tiny day by day. According to Moore's law, the device size gets smaller to increase transistor count and circuit speeds [1], leading to high power dissipation and heat fluxes. Thus, thermal management of such devices like laser diode, supercomputer, military devices, and light emitting diode systems has become extremely challenging for safe and reliable operations [2,3]. In addition, on-chip power management and high-performance demands in recent years have increased the nonuniformity of chip power dissipation, resulting in highly localized hot spots at submillimeter scales. The conventional cooling technique, such as natural or forced air cooling, has become insufficient for devices exceeding a heat flux of 1 W/cm^2 [4]. New and novel cooling techniques are in need to selectively cool submillimeter hot spots, while providing effective global cooling [3]. Two-phase flow boiling with microchannel heat sinks is known as an effective cooling solution for such applications as it has the potential to remove a substantial amount of heat with the large latent heat of vaporization absorbed by the liquid coolant during phase change [5]. It can also maintain a more uniform wall temperature and requires less pumping power compared to a single-phase coolant for equivalent performance [6]. Despite the benefits of dissipating higher heat flux, two-phase flow boiling in microspaces encounters some critical problems like flow instability, premature dry out, lower heat transfer coefficient, and pressure drop during boiling [7–10].

The flow boiling in the microchannel can be affected by varying flow patterns such as bubbly, slug, churn, and annular flow or a combination of these [11]. Inside the microchannel, temporary vapor blockage and subsequent pressure peak can be happened with quick evaporation of bubbles [12], resulting in reverse flow or even local dry patches [13]. The accumulation of bubbles at downstream decreases the mass flux, resulting in pressure drop and an increase in wall temperature [14]. The flow reversal phenomenon is also observed due to upstream and downstream vapor [15,16]. Additionally, high inlet compressibility [17] and location of boiling incipience [12] can cause flow instability. Various techniques such as flow restrictor at inlet [18,19], diverging or expanding microchannel [20–22], transverse direction cross-connected microchannels [23], and artificial nucleation sites [24,25] have been proposed to improve flow stability. While inlet restrictors reduce backflow [18] and artificial nucleation sites increase heat transfer [24], both induce additional pressure instability. Moreover, high wall temperature and dry patches issues still remain unresolved with these techniques. The wall temperature can be more critical when considering a local hot spot in microchannel flow. Local hot spot forms in electronic devices, resulting in a significant rise in peak temperature at the same power level. The microgap heat sink shows good potential to mitigate local hotspots as it provides extra room for vapors to expand in the transverse and downstream direction and also maintains uniform pressure and fluid film on the hot surface. Alam et al. [26] studied microchannel and microgap heat sinks and found that the microgap channel provides uniform wall temperature with lower temperature fluctuations. It also mitigates the hot spot. The numerical

---

[1] Corresponding author.

Contributed by the Heat Transfer Division of ASME for publication in the Journal of Heat Transfer. Manuscript received December 7, 2020; final manuscript received June 23, 2021; published online July 21, 2021. Editor: Portonovo S. Ayyaswamy.

investigation of Bar-Cohen and Wang [3] showed the efficiency of microgap heat sink. They found that proper thermal, electrical, and geometric optimizations yield hot spot temperature reductions of more than 17 °C at a 400 μm × 400 μm 1250 W/cm^2 hot spot. The hot spot cooling performance using microgap is also studied using different geometries and coolants [27–32]. The 2D flow visualization on microgap heat sink shows different flow patterns such as bubbly, intermittent, slug, and annular flow depending on gap size [28,33]. Alam et al. [30] found that confined slug and annular boiling are the dominant heat transfer mechanisms in microgap channels and the heat transfer coefficient increases as the gap size decreases.

One of the main causes of flow instability is the presence of vapor or dry patches in the flow path. The effect of vapor or dry patches in the microchannel can be reduced by rewetting on the surface [14,34,35]. This indicates the potential of the hydrophilic surface to reduce the flow instability in microchannel flow boiling. In a macroscale, external force dominates over surface force in the study of flow boiling on the wetting surface, while surface force becomes significant in the microscale. Trieu Phan et al. [36] investigated the flow boiling with varying wettability (26 deg, 49 deg, 63 deg, and 104 deg). They concluded that two-phase pressure drop increases up to 170% from hydrophilic to hydrophobic surface. The microchannel coated with carbon nanotube [37], silicon nanowires [38–40], and copper nanowires [41] shows improvement in wettability and capillarity, which increases heat transfer coefficient while reducing pressure drop as well as flow instability. Choi et al. [42] fabricated hydrophilic and hydrophobic microchannel using chemically treated glass. Their visualization study showed that short elongated bubbles are formed at low vapor quality and long elongated bubbles are dominant flow patterns at high vapor quality. They also claimed that hydrophilic surface increased heat transfer efficiency at low vapor quality by rewetting the liquid film during local dry out. Liu et al. [43] studied the characteristics of flow boiling on hydrophobic to superhydrophilic microchannels. They observed that on the hydrophilic surface ($\theta \sim 36$ deg) new bubbles liked to nucleate, grow, and coalesce into an elongated bubble and then flushed away with incoming water periodically. For the hydrophobic surface ($\theta = 103$ deg), only elongated bubbles formed at higher superheat compared to a hydrophilic surface. The heat transfer coefficient is higher for hydrophilic microchannel compared to hydrophobic at low vapor quality and low heat flux but opposite for high vapor quality and heat flux [43,44]. Besides pure hydrophilic and hydrophobic surfaces, some studies showed the excellence of mixed or patterned hydrophilic surfaces in microchannel flow boiling [45–47]. However, mechanisms behind improved heat transfer performance have not been well understood due to the complexity from different factors such as bubble departure, nucleation site density, critical heat flux, heat transfer coefficient, capillarity, and channel geometry in the microchannel flow boiling [45]. So, it is important to understand the effect of wettability in a particular microscale flow system.

Another weakness in two-phase flow behavior is a strong reliance on empirical correlations for predicting two-phase activity in microgaps. Due to the lack of any quantitative standards, the flow boiling correlation outside a specific operating condition does not work accurately [31]. Artificial neural network (ANN) is a computing system that solves problems by imitating mechanisms of the human brain. It has been applied to various engineering applications, including convective heat transfer [48–52] and boiling [53–58] to estimate desired performance parameters with adequate experimental data. Scalabrin et al. [53,54] modeled heat transfer of flow boiling in horizontal tubes for different fluids using ANN and found that the flow boiling heat transfer model does not fundamentally depend on the flow pattern. They also showed that the ANN predicted data are more accurate in consideration of the experimental uncertainties. Naphon et al. [59] investigated jet impingement nanofluid in microchannel and found that there was only 1.25% error between experimental and ANN prediction. Recently, ANN-based predicting model of mini/microchannel flow boiling heat transfer with a consolidated dataset (using 50 data sources) is developed by Qiu et al. [60]. They concluded that their prediction model works better when the operating fluid is included in the training data. While ANNs have shown good promise in predicting thermal characteristics across many thermal systems, this method has not yet been implemented to predict complex microchannel or microgap flow boiling heat transfer.

In this study, we used the microgap heat sink with an enhanced surface wettability to characterize the flow boiling heat transfer. To the best of our knowledge, it has not been studied yet. The main objective of this study is to characterize the flow boiling performance and hotspot mitigation on microgap heat sink with enhanced surface wettability and compare it with conventional (nonwetting) heat sink. The experiment is carried out for a range of heat flux (q) varying from 91.35 kW/m^2 to 118.25 kW/m^2 and mass flux (j) varying from 1.656 kg/m^2 s to 4.97 kg/m^2 s. The operating map of Hong et al. [61] for stable/unstable flow boiling regime for de-ionized (DI) water in micro/minichannels heat sink illustrates that unstable flow boiling always occurs at $q/j > 1.01$ kJ/kg and $q < 700$ kW/m^2, and in most of the previous studies the low flow inertia and high vapor quality region is ignored. The heat flux and mass flux ranges in this study cover the low flow/mass flux and high vapor quality region. Moreover, we predict the two-phase heat transfer coefficient using ANN tool for this microgap system.

2 Experimental Setup and Methodology

2.1 Flow Loop and Test Module. Figure 1 shows the schematic diagram and picture of the experimental setup. It uses an open loop system with DI water supplied to the stainless steel (SS) heat sink. The water flow is regulated by a syringe pump (NE-1000X, New Era, Farmingdale, NY). The temperature and pressure are measured before and after the water passes the SS heat sink using T-type thermocouple and absolute pressure sensor (PX219-200A5V, Omega, Norwalk, CT), respectively. The inlet temperature ranges from 21 °C to 22 °C for all experiments. A differential pressure sensor (PX419-015DWUV, Omega, Norwalk, CT) is set to measure the pressure difference between inlet and outlet. The test piece is comprised of Teflon base plate, polycarbonate top cover, 27 mm × 27 mm SS plate, and leaded resistor (heater) as illustrated in Fig. 2(*a*). The SS metal plate has a shallow channel with a depth of 170 μm and width of 19.8 mm. The SS plate is used to generate a hot spot due to its low thermal conductivity. A 150 W thick film resistor (R1000-150-4E, Barry Industries Inc., Attleboro, MA) mounted on the Teflon base is used as a heater which is 8.89 mm long and 5.84 mm wide. A thermal compound (Chemplex® 1381 DE, Fuchs Lubricants, Harvey, IL) is applied on the heater surface to maintain constant conduction between heater and heat sink. Two 7.62 mm holes are drilled through the Teflon base plate just before inlet and after outlet to attach two absolute and one differential pressure transducer. Power is supplied to heater using a DC source. As shown in Fig. 2(*b*), ten T-type thermocouples are installed to measure the temperature of the heat sink (SS plate) surface at different positions: eight (1–8) are measuring the local temperature of metal plate from bottom, one (h) is located in between the heater and metal plate, and the other one (t) is fixed through top polycarbonate part to measure the flowing water temperature right above the SS metal plate. Two more thermocouples, attached to the polycarbonate part, are used to measure the inlet and outlet temperature. The data acquisition (DAQ) system (Agilent 34970A, Agilent, Santa Clara, CA) records all temperature and pressure data.

2.2 Fabrication of Hydrophilic Surface on Heat Sink. The SS microgap heat sink configuration is shown in Fig. 3(*a*). The channel dimensions denoted by a, b, and c are 20 mm, 27 mm, and 170 μm, respectively. Two different geometries of hydrophilic surface are prepared on the microgap channel: (1) particle

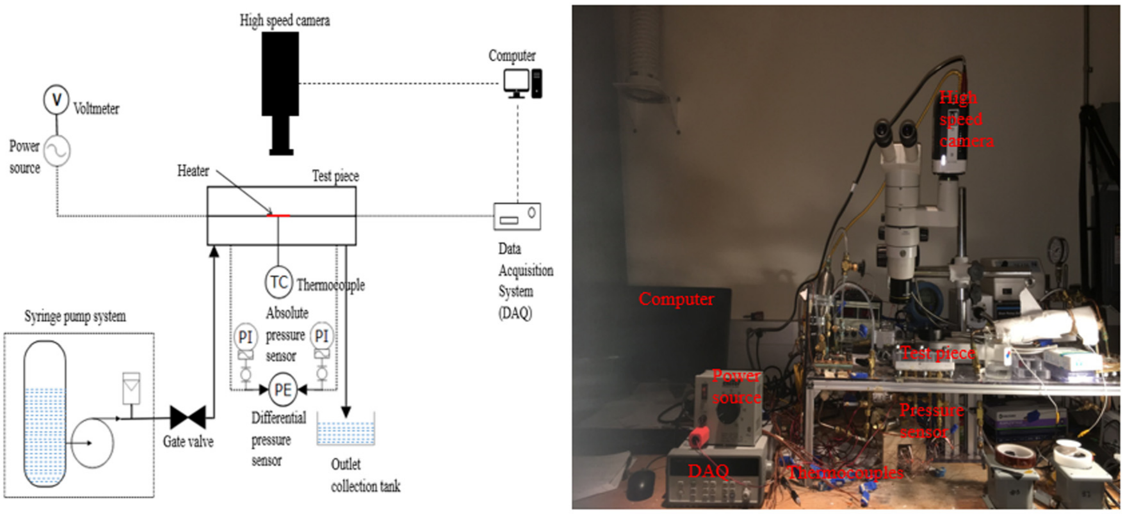

(*a*) (*b*)

Fig. 1 (*a*) Schematic diagram of experimental setup and (*b*) picture of real experimental setup

hydrophilic (Fig. 3(*b*)) and (2) channel hydrophilic (Fig. 3(*c*)). They both are treated in the same way for the hydrophilic coating, but differ in the coverage area. The area of the partial hydrophilic surface corresponds to the hot spot generated by the heater on the SS plate, which is 8.89 mm × 5.84 mm. The full length of the heat sink (27 mm) with the same width of hot spot (5.84 mm) is treated to prepare the channel hydrophilic surface. To fabricate the hydrophilic surface, a 200 nm thick film of SiO_2 is deposited on the SS heat sink using a sputtering system (Nano 36^{TM} Kurt J Lesker, Jefferson Hills, PA). The treated surface is characterized by a goniometer (rame-hart 200 goniometer, Succasunna, NJ). The average contact angle (CA) for a conventional (nontreated) SS plate is ∼87 deg which drops to ∼8 deg after treatment.

2.3 Test Procedure. Both conventional and hydrophilic microgap heat sinks are tested with DI water having inlet temperature of 21.5 °C. At the beginning, the heat sink is set to the test piece, and the test section is connected to the flow loop. The power supply is connected to the heater and maintained at the same power level throughout the experiment. Once all the thermocouple and pressure readings reach steady-state condition (after an hour), the syringe pump is started to flow water. Three different flow rates, 0.5 ml/min, 1 ml/min, and 1.5 ml/min, are used to see the cooling effect. The experiment is repeated for different heat fluxes ranging from 83.15 to 118.25 kW/m^2. All the temperature and pressure data are captured in the DAQ (Agilent 34970A, Agilent, Santa Clara, CA) system. The DAQ scanning time is set to 100 ms. A high-speed camera (Miro M310, Phantom, Wayne, NJ) is also used to visualize the morphological change inside bubbles during flow boiling. The CA is measured before and after each test to check the change in hydrophilicity.

2.4 Data Reduction. In this experiment, the input power (P) of the DC power source is calculated using input voltage (V) and current (I)

$$P = VI \tag{1}$$

Heat transfer rate (Q) is calculated considering the heat loss (Q_{loss}) to surrounding ambient. Some heat is lost through the heat sink of the microheater. The average heat loss with the microheater is around 9% of input power P at more than 150 °C operating temperature according to microheater specification

$$Q = P - Q_{\mathrm{loss}} \tag{2}$$

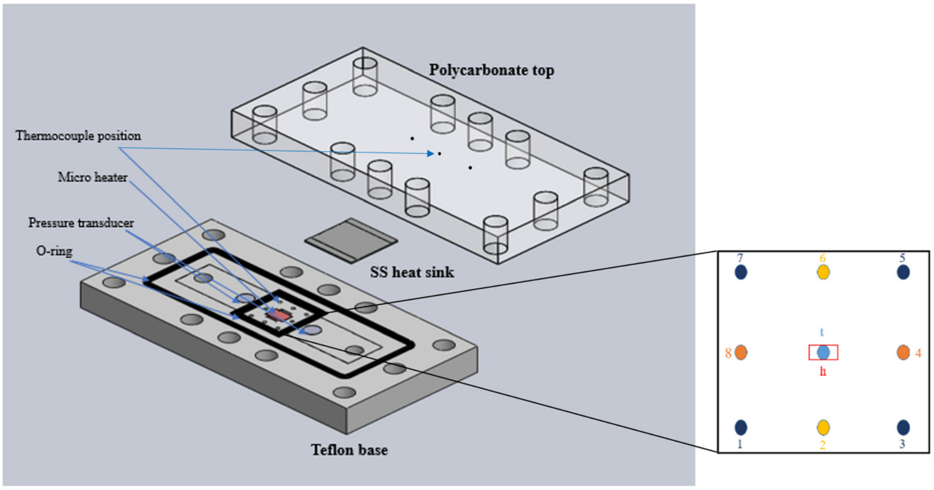

(*a*) (*b*)

Fig. 2 (*a*) Split view of test section and (*b*) thermocouple positions under heat sink

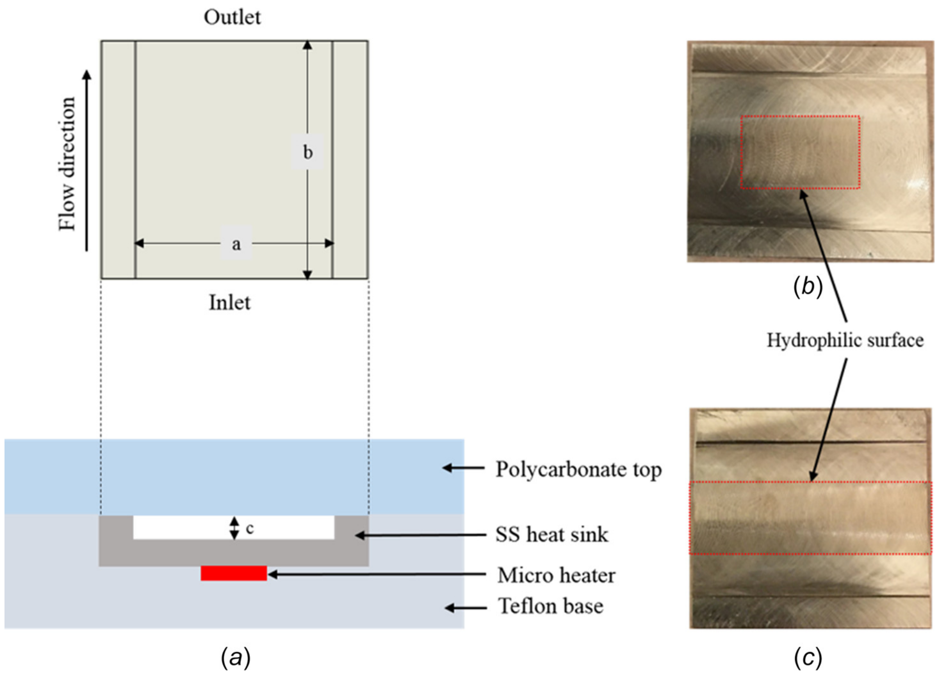

Fig. 3 (*a*) Schematic diagram of microgap test section, and hydrophilic treated microgap (*b*) partial hydrophilic, and (*c*) channel hydrophilic heat sink

Two-dimensional temperature difference (ΔT) is calculated using average wall temperature (T_s) and average saturated water temperature at outlet (T_w) when the temperature reaches steady-state during cooling

$$\Delta T = T_s - T_w \tag{3}$$

The microheater's surface area (A_h) is considered to calculate effective heat flux (q)

$$q = \frac{Q}{A_h} \tag{4}$$

The two-phase heat transfer coefficient (h) can be calculated using

$$h = \frac{q}{\Delta T} \tag{5}$$

As the test section maintains the same width, the contraction and expansion pressure loss is minimal compared to the microgap pressure loss. Pressure drop (ΔP) is measured from the differential pressure sensor data.

2.5 Uncertainty Analysis. The uncertainty analysis is done using normal error distribution. As there is a variation in experiment time and repeatability, statistical uncertainty is considered with 95% confidence level. The following statistical uncertainty formula is used to calculate the uncertainty in temperature and pressure:

$$\Delta x = \frac{1.96 \times \sigma}{\sqrt{N}} \tag{6}$$

where Δx is uncertainty, σ is the standard deviation, and N is the number of samples.

The uncertainty of two-phase heat transfer coefficient can be calculated using the following equations:

$$\Delta h = \sqrt{\left(\frac{1}{T_s - T_w}\delta q\right)^2 + \left(\frac{q}{(T_s - T_w)^2}\delta T_s\right)^2 + \left(\frac{q}{(T_s - T_w)^2}\delta T_w\right)^2} \tag{7}$$

where Δh is the uncertainty in heat transfer coefficient, and δq, δT_s, and δT_w are the uncertainties in heat flux, saturated wall temperature, and saturated water temperature, respectively.

The uncertainties from the manufacturer for different parameters and sensors are shown in Table 1.

3 Artificial Neural Network Theory

Artificial neural network is a deep learning tool that adopts a mathematical or computational process mimicking the learning process of the human brain. McCulloch and Pitts first proposed it in 1943 [62]. ANN has an intelligent adaptive system that can reconfigure itself in the learning process, based on external or internal knowledge that flows through the network. It is widely used as a statistical prediction tool due to its adaptability, learning capability, nonlinearity, input–output mapping, and fault tolerance [63]. As ANN maps provide an approximate model according to given data, it can be applied to problems with no algorithmic solutions or with too complex algorithmic solutions. In general, ANN architecture consists of three layers, including the input layer, hidden layer, and output layer. Each layer has a number of connected nodes, called artificial neurons. The strength of the connected neurons is defined by weight. Each neuron accepts a weighted set of inputs and gives an output response through an activation function. A set of connection weights and biases need to be adjusted to enable the network for the required task. The activation function processes the sum of weighted inputs with a bias. Different types of activation functions can be used, such as hard limit threshold function, log-sigmoid function, and hyperbolic tangent function. A particular function is performed by adjusting the connection values, i.e., weights and biases, during the ANN training process. The training continues until it reaches an accepted degree of accuracy. In other words, the weights and biases are modified to minimize the error between the output of the network and the desired output. When the error falls below a predetermined threshold or exceeds the maximum number of epochs, the training process will cease. One epoch of training is typically defined as a single presentation of all input vectors to the network [56]. In this study, a multilayer feed-forward neural network is built, in which all layer nodes are connected to all other nodes of the preceding and subsequent layers.

3.1 Artificial Neural Network Modeling. The ANN adopts a learning algorithm to execute the training process. The backpropagation algorithm, a widely used algorithm in ANN for engineering problems, is adopted here. In this algorithm, the input data are forwarded via the transfer function, and errors are propagated backward. The Levenberg–Marquardt optimization technique is used to adjust the weights and biases. The network learns through the gradient descent algorithm with momentum. A log-sigmoid (LOGSIG) activation function is applied to the hidden layer, which adjusts the neuron's connection value (weights and biases)

$$\mathrm{LOGSIG}(X) = \frac{1}{1+e^{-X}} \tag{8}$$

where X is any input value. In this study, five different inputs and one output data are used, which have varying data ranges. For accuracy and simplicity, all input and output data are normalized (X_n) within 0 to 1 and then return to the original value after prediction

$$X_n = \frac{X - \min(X)}{\max(X) - \min(X)} \tag{9}$$

Each neuron accepts a weighted set of inputs and gives an output response. Such a neuron initially forms the sum of weighted inputs (V)

$$V = \sum_{i=1}^{n} (w_i X_i) + b \tag{10}$$

where n is the number of elements, w_i is the interconnection weights of input vector X_i, and b is the bias for the neuron. Weight is updated in each iteration based on the learning rate [52]

$$w_i^{\text{new}} = w_i^{\text{old}} - \eta \frac{\delta E}{\delta w_i} \tag{11}$$

where η is the learning rate, and $\delta E/\delta w_i$ is the gradient of error. In the backpropagation process, error acts as a driving parameter as it determines the end of training when error becomes minimum. Error deviation can be evaluated as

$$k_e = \frac{E}{k_d} = \frac{k_p - k_d}{k_d} \tag{12}$$

where k_p represents the predicted or calculated output, and k_d represents the desired or expected output. To compare the performance of different ANN architecture, mean relative error (MRE) and standard deviation of relative error (STD_R) are evaluated [64]

$$\mathrm{MRE} = \frac{1}{n} \sum_{i=1}^{n} k_e \tag{13}$$

$$\mathrm{STD}_R = \sqrt{\sum_{i=1}^{n} \frac{(k_e - \bar{k}_e)^2}{n-1}} \tag{14}$$

Table 1 Measurement accuracies and experimental uncertainties associated with sensors

Sensors and parameters	Accuracies and uncertainties
T-type thermocouple	±1 °C
Absolute pressure sensor	±3.44 kPa
Differential pressure sensor	±0.103 kPa
SS heat sink depth	±35 μm
Power source (voltage, current)	±0.06 V, ±0.15 A
Resistor or microheater	±5%
Heat flux	5–8%
Pressure drop	8–14%
Heat transfer coefficient	7–12%

4 Results and Discussion

In this study, flow behaviors are visualized during flow boiling using a high-speed camera for three different sample types: conventional (nontreated), partially hydrophilic, and channel hydrophilic surfaces. The relative comparisons in flow regimes along with temperature and pressure change for three different samples are presented for various mass and heat fluxes to differentiate the bubble characteristics, stability, hotspot mitigation, and heat transfer performance. The wettability change for hydrophilic surfaces is also characterized by the contact angle measurement.

4.1 Flow Visualization. Figures 4–6 summarize the flow patterns with corresponding temperature and pressure changes for the heat flux of 99.93 kW/m^2 and mass flux of 3.31 kg/m^2 s on three different heat sinks, conventional, partial hydrophilic, and channel hydrophilic, respectively. To compared flow patterns for three different heat sinks, the visualization is focused on two stages: initial cooling (Z1) and saturated cooling (Z2). At the beginning of cooling, vapor film initiates on hot spot which lasts longer on conventional surface ($t = t_0 + 95.04$ s) compared to partial hydrophilic ($t = t_0 + 0.416$ s) and channel hydrophilic ($t = t_0 + 0.125$ s) heat sink. It indicates that local dry out prevails for a longer period on the conventional surface. A short peak appears in the temperature just right after the initiation of cooling at the initial stage, Z1, due to the presence of vapor film on the conventional surface. The wall temperature also increases on the conventional surface due to a lack of water supply. Moreover, fluctuations or cyclic patterns are observed in the temperature profile of the conventional surface due to belated rewetting.

On the other hand, hydrophilic surfaces can maintain low wall temperature with less fluctuation due to frequent rewetting. Among the hydrophilic surfaces, the channel hydrophilic heat sink mitigates hot spot temperature better with the least fluctuation. Rewetting phenomena are also responsible for pressure variations on conventional and hydrophilic heat sinks. The pressure is more consistent (less fluctuation) on channel hydrophilic as it has high water availability due to the most frequent rewetting, compared to the partial hydrophilic and conventional heat sink. It should be noted that differential pressure is higher on hydrophilic surfaces compared to conventional one due to the presence of a consistent water supply. The hydrophilic surface has a higher water affinity that helps to flush vapor film out from the hot spots just in a fraction of seconds. Thus, there is no increase in temperature after initiating water flow. After initial vapor flushing, new bubbles form and coalesce to create bubble clusters or slugs. The slug flow is found to be the dominant flow pattern in this study. Because of low water content, the vapor slug acts as an insulation layer and resists heat transfer. So, the presence of a larger slug increases the temperature on the hot spot. To mitigate hot spot temperature, slug flushing plays a significant role. Slug forms and flushes repeatedly when the temperature becomes close to saturation. The comparison of Figs. 4–6 shows that slugs' flushing varies with surface wettability. It is evident from these visualizations that the quickest slug removal happens on channel hydrophilic ($t = t_0 + 39.82$ s) followed by partial hydrophilic ($t = t_0 + 47.86$ s) and then conventional ($t = t_0 + 55.58$ s) heat

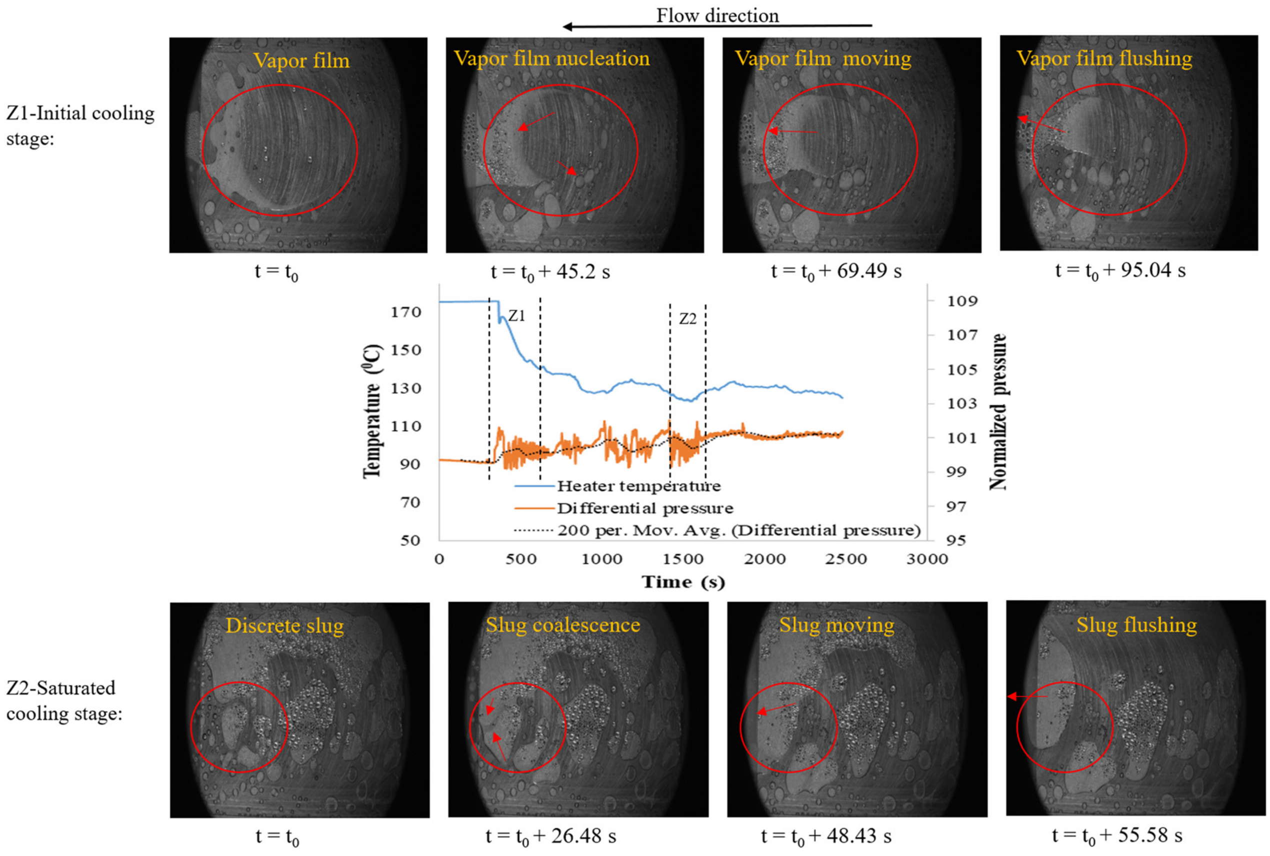

Fig. 4 Change in flow pattern with temperature and pressure on conventional heat sink at $q = 99.93$ kW/m^2 and $j = 3.31$ kg/m^2 s

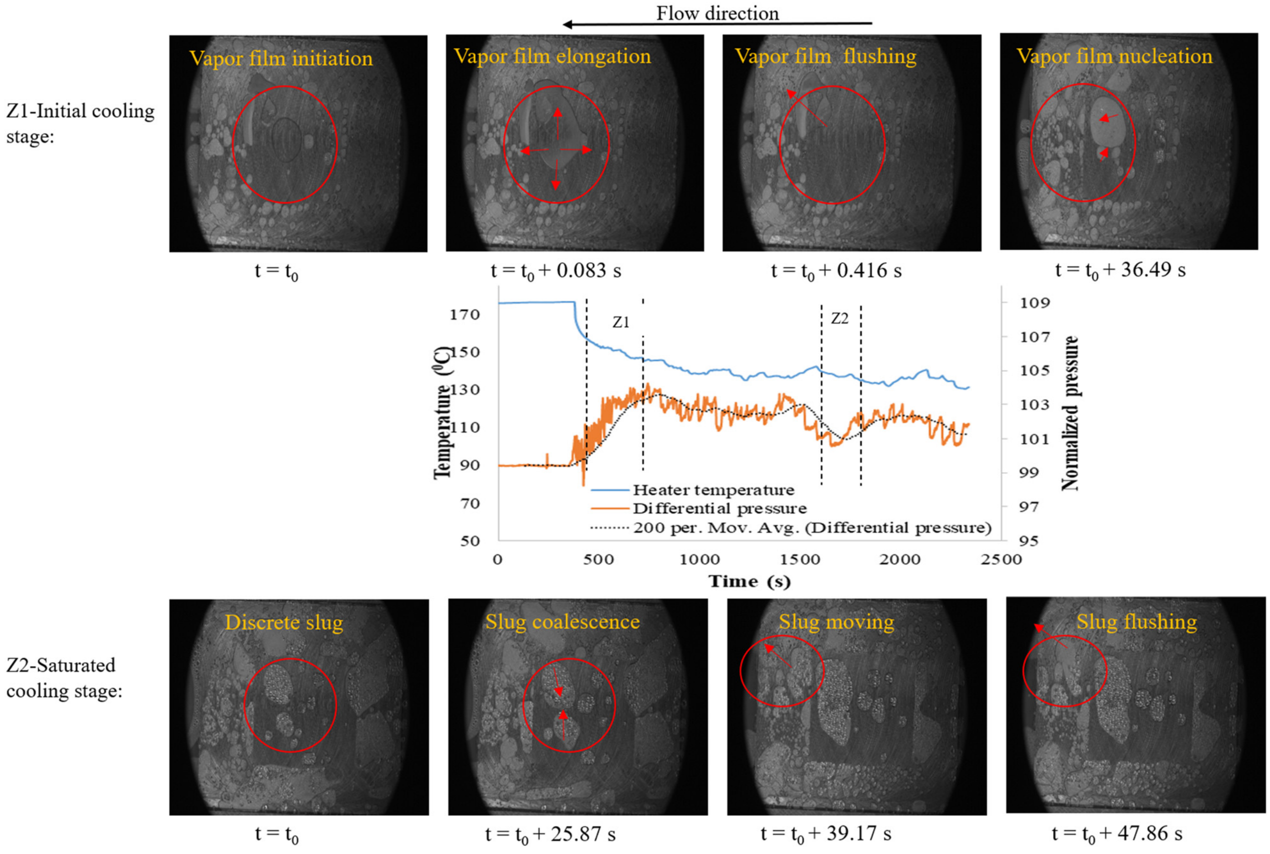

Fig. 5 Change in flow pattern with temperature and pressure on partially hydrophilic heat sink at $q = 99.93$ kW/m^2 and $j = 3.31$ kg/m^2 s

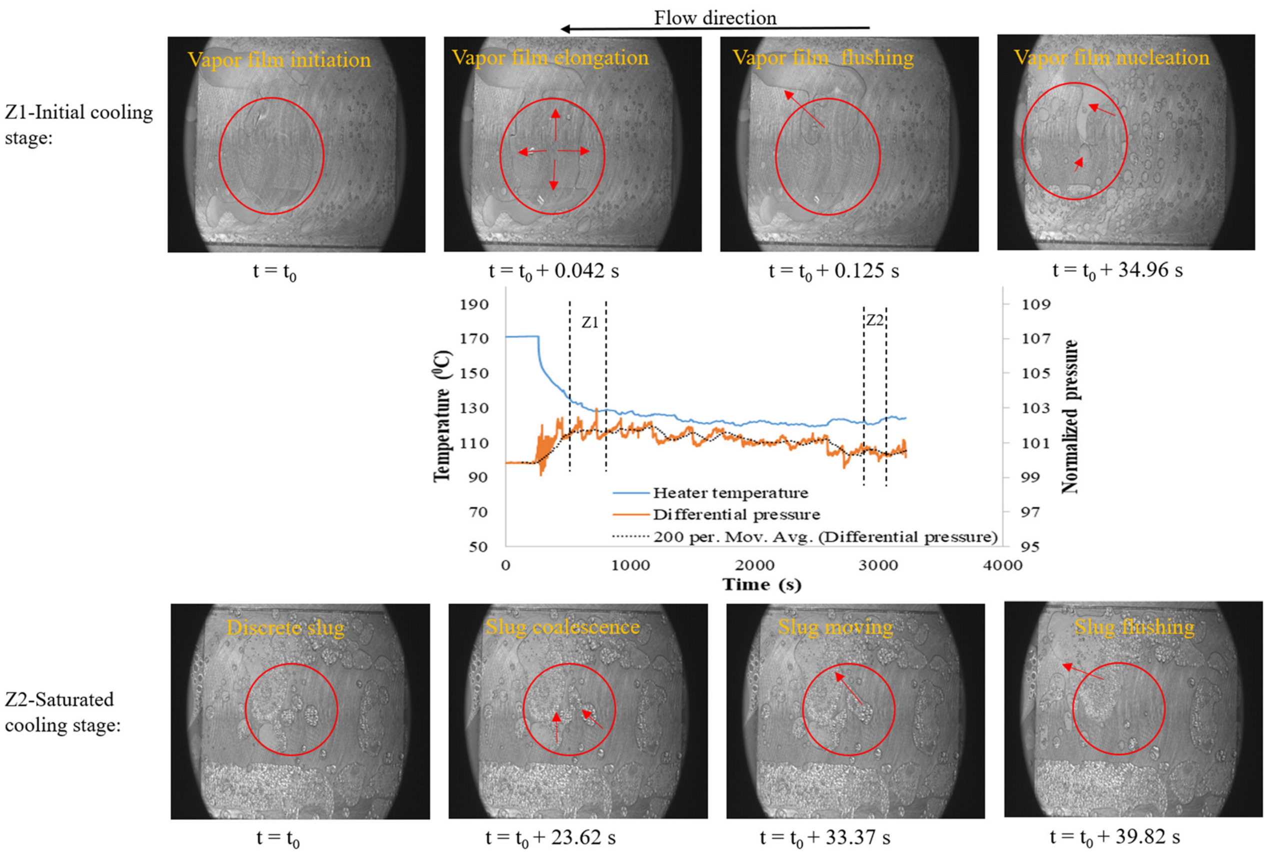

Fig. 6 Change in flow pattern with temperature and pressure on channel hydrophilic heat sink at $q = 99.93$ kW/m^2 and $j = 3.31$ kg/m^2 s

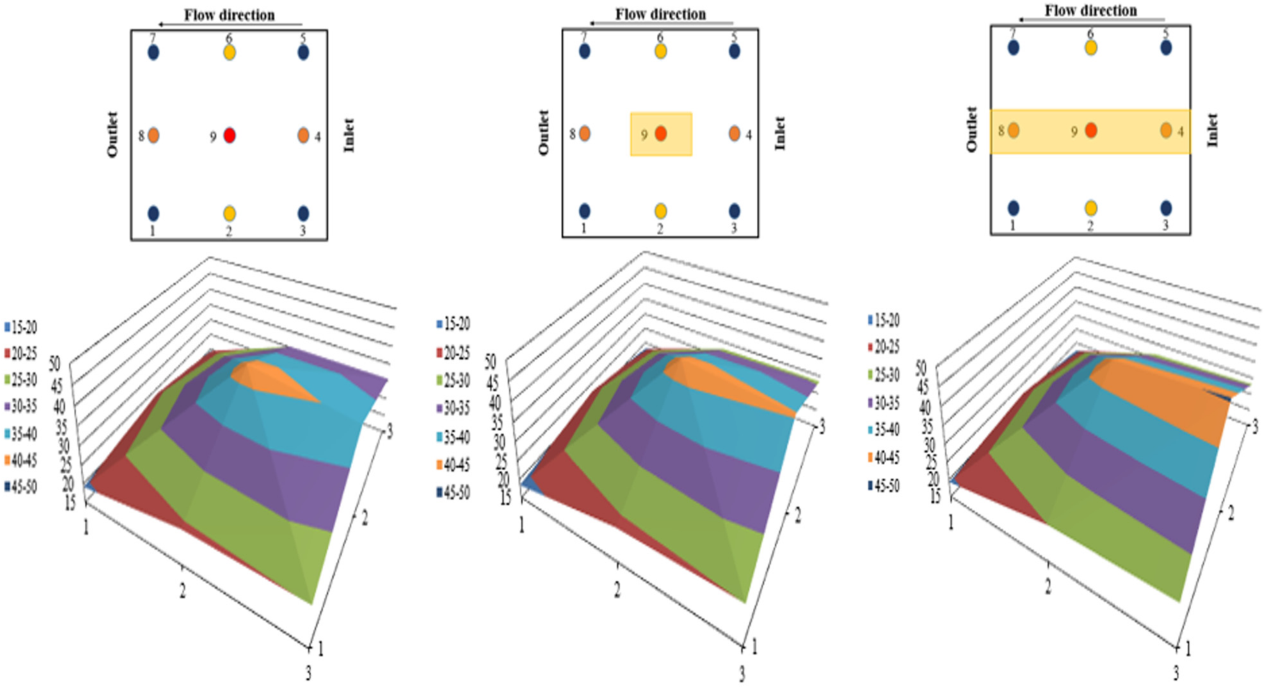

(*a*) (*b*) (*c*)

Fig. 7 2D temperature drop after cooling at nine different positions for $q = 91.35$ kW/m^2 and $j = 3.31$ kg/m^2 s on (*a*) conventional, (*b*) partial hydrophilic, and (*c*) channel hydrophilic heat sink. The rectangular shaded area represents the hydrophilic region on each heat sink.

sink. The slugs are more easily removed by rewetting or new incoming water with hydrophilic surfaces. The full channel hydrophilic surface creates a smooth route for the water to pass through the hot spot, resulting in easy removal of slugs. However, stationary slugs at the nonhydrophilic upstream block the passage of water flow on both conventional and partial hydrophilic surfaces. So, it resists the incoming water and hinders water flow. Additionally, due to the expansion and shrinkage of the vapor slugs, pressure fluctuates more on surfaces having nonhydrophilic downstream, i.e., conventional and partial hydrophilic surfaces. With less interrupted flow path and pressure fluctuation, the channel hydrophilic surface improves heat transfer and hot spot mitigation.

4.2 Hotspot Mitigation. In this study, the SS plate is used as a heat sink to check the hot spot mitigation capabilities of different microgap heat sinks due to its nonuniform heat flux distributions like electronic chips. The temperature of the heat sink is measured at nine different positions (indicating 1–9 in Fig. 7) using thermocouples to understand the local cooling effect. The surface plots in Fig. 7 illustrate the relative temperature drop after cooling for $q = 91.35\,\mathrm{kW/m^2}$ and $j = 3.31\,\mathrm{kg/m^2\,s}$ for conventional, partial hydrophilic, and channel hydrophilic heat sinks. It also represents the overall local cooling performance on each heat sink. The thermocouple position, 9, represents the hot spot and maximum temperature drop (denoted by orange color region) is found around this position. The maximum temperature drop region in the 3D temperature plots increases gradually from conventional to channel hydrophilic surface indicating temperature drop or heat transfer increase. The temperature drops after cooling at position 9 on conventional, partial hydrophilic, and channel hydrophilic heat sink are 42.43 °C, 42.73 °C, and 43.65 °C, respectively, which is a clear indication of the highest temperature drop with channel hydrophilic heat sink. It is also evident that the area of high-temperature color legends is larger for channel hydrophilic heat sink compared to others. The visualization shows frequent rewetting and smooth progression of water on channel hydrophilic heat sink helps to mitigate hot spot temperature.

4.3 Two-Phase Heat Transfer. The two-phase heat transfer coefficient is calculated using the temperature difference between the hot spot on the heat sink and saturated water at the outlet. Figure 8(*a*) shows the variation of the heat transfer coefficient with heat fluxes on conventional, partial, and channel hydrophilic heat sink for the mass flux of $1.656\,\mathrm{kg/m^2\,s}$. The heat transfer coefficient increases more for hydrophilic surfaces compared to conventional at a low flow rate or mass flux. The improvement is more noticeable at high heat flux ($>99.93\,\mathrm{kW/m^2}$). Due to the low flow rate and high heat flux, water does not like to flow over the hot spot region, especially on the conventional heat sink. However, the hydrophilic surfaces facilitate to overcome this issue by attracting more water on the hot spot. At mass flux of $3.31\,\mathrm{kg/m^2\,s}$ in Fig. 8(*b*), the heat transfer coefficient trends for all surfaces are descending with an exception for the conventional surface at high heat flux ($118.25\,\mathrm{kW/m^2}$). The consistent improvement in the heat transfer coefficient on channel hydrophilic heat sink is shown for the mass flux of $4.97\,\mathrm{kg/m^2\,s}$ in Fig. 8(*c*). The trends for partial and channel hydrophilic at $3.31\,\mathrm{kg/m^2\,s}$ and $4.97\,\mathrm{kg/m^2\,s}$ are similar and descending at high heat fluxes, which is opposite to the conventional surface. It has been observed that the heat transfer coefficient decreases on the hydrophilic surface at higher vapor quality or heat flux [42,44,65]. According to Trieu Phan et al. [44], heat transfer through conduction from a hot surface to a thin liquid layer remains on the hydrophilic surface at high heat flux. This thin layer is affected by different factors such as the shear force at the liquid–vapor interface, the evaporation rate, and the capillary effect. As capillary action is dominant on microscale hydrophilic surface, it retains thin liquid film unchanged, and so heat transfer does not improve at high heat flux or vapor quality.

The heat transfer coefficient increases on channel hydrophilic heat sink around 5–12% at $3.31\,\mathrm{kg/m^2\,s}$ and 7–14% at $4.97\,\mathrm{kg/m^2\,s}$ compared to the conventional heat sink at low heat fluxes ($<108.9\,\mathrm{kW/m^2}$). Again, the heat transfer coefficient increases on channel hydrophilic heat sink around 2–10% at $3.31\,\mathrm{kg/m^2\,s}$ and 4–9% at $4.97\,\mathrm{kg/m^2\,s}$ compared to the partial hydrophilic heat sink at low heat fluxes ($<108.9\,\mathrm{kW/m^2}$).

4.4 Two-Phase Pressure Change. Two-phase pressure change is measured from the differential pressure sensor, which is set inside the test piece. As the width of the flow channel is uniform (no sharp contraction and expansion) everywhere and mass fluxes used in cooling are low ($1.656\,\mathrm{kg/m^2\,s}$, $3.31\,\mathrm{kg/m^2\,s}$, and $4.97\,\mathrm{kg/m^2\,s}$), we assume that the friction losses are negligible. The differential pressure readings are normalized with respect to 100 kPa due to the measurement variations of initial conditions in each test. In two-phase cooling in microspace, pressure fluctuation occurs due to the expansion and contraction with bubbles forming and collapsing. To represent pressure drop for a single flow rate at a specific heat flux, an average of approximately 1200 differential pressure data is taken at the steady-state.

Figure 9 shows the normalized pressure change with respect to heat flux for different mass fluxes on conventional, partial hydrophilic, and channel hydrophilic heat sink. Among three mass

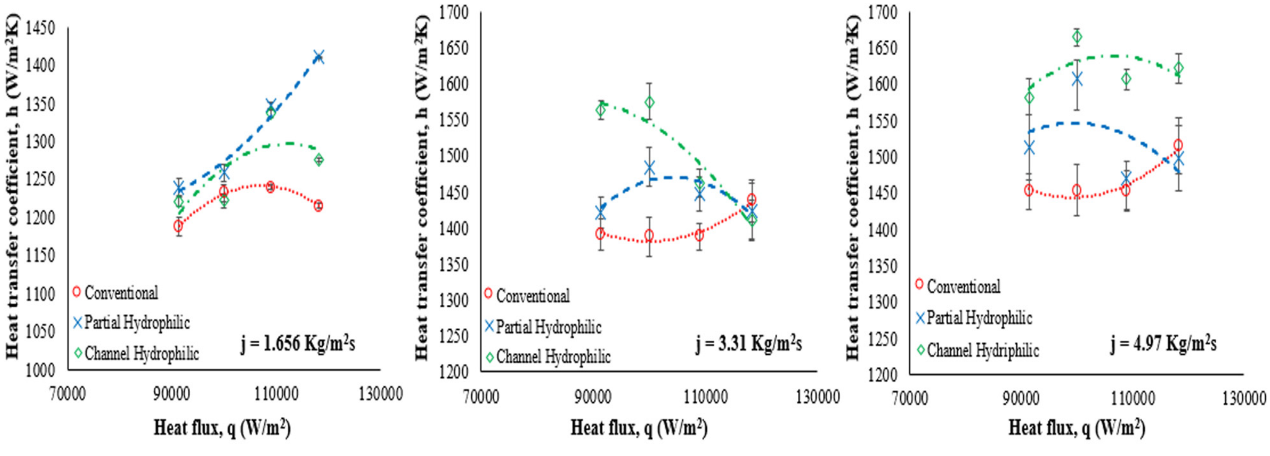

(*a*) (*b*) (*c*)

Fig. 8 Variation of heat transfer coefficient with heat fluxes on conventional, partial, and channel hydrophilic heat sink for mass flux of (*a*) $1.656\,\mathrm{kg/m^2\,s}$, (*b*) $3.31\,\mathrm{kg/m^2\,s}$, and (*c*) $4.97\,\mathrm{kg/m^2\,s}$

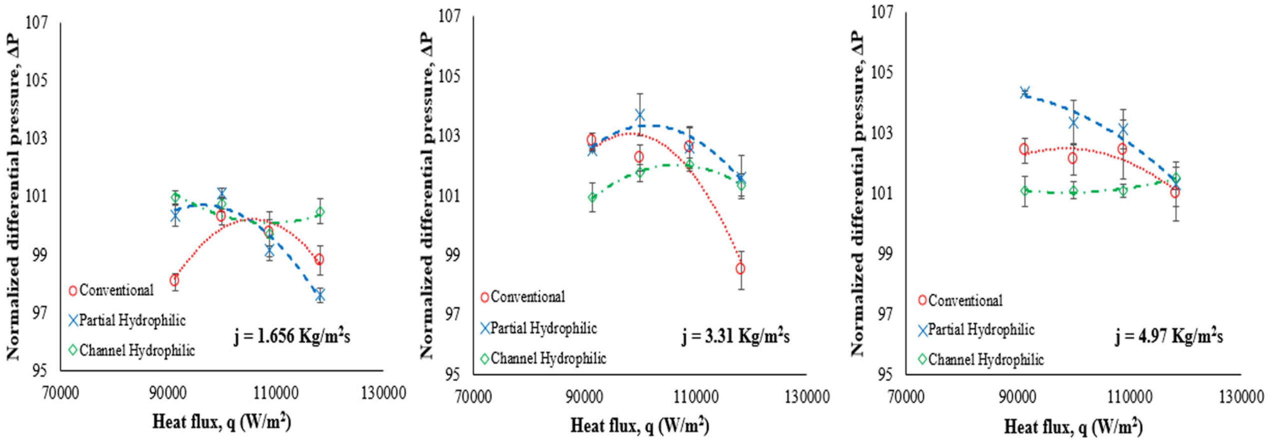

(*a*) (*b*) (*c*)

Fig. 9 Variation of normalized pressure drop with heat fluxes on conventional, partial, and channel hydrophilic heat sink for mass flux of (*a*) 1.656 kg/m^2 s, (*b*) 3.31 kg/m^2 s, and (*c*) 4.97 kg/m^2 s

fluxes in this study, the relatively smaller variation in pressure drop is observed at the highest mass flux (4.97 kg/m^2 s) across the range of heat fluxes, which is partly because slugs cannot stay on the hot spot for a long time. It is also seen that normalized differential pressure at a high heat flux decreases on conventional and partial hydrophilic heat sinks for all three mass fluxes due to the increase of vapor. The presence of vapor on the hot spot resists the water flow, leading to a decrease in pressure. On the channel hydrophilic heat sink, differential pressure is more consistent for all three mass fluxes. The small pressure variation on the channel hydrophilic results from the less interrupted flow along the heat sink by hydrophilic surface. It also quickly removes slugs and vapor from the hot spot to minimize the pressure build-up, resulting in the prevention of pressure instability. For the partial hydrophilic surface, the differential pressure is showing a relatively large variation for all three mass fluxes compared to conventional and channel hydrophilic surfaces. It may be attributed to the longer stay of vapor slugs on the nontreated area near the outlet and at the interface between the treated and the nontreated surface.

4.5 Wettability Change During Flow Boiling. To examine the change in wettability of the hydrophilic surface, the CA is measured before and after each test. Figure 10 shows the change of CA for various heat and mass fluxes. The solid columns represent the CA before the test, and the blank columns represent the CA after the test. The results indicate that the hydrophilicity degrades for both partial and channel hydrophilic surfaces after the flow boiling test. The largest increment in CA occurs for both partial and channel hydrophilic surfaces at a low mass flux (1.656 kg/m^2 s). We attribute the large increment in CA to an extended stay of bubbles and slugs on the hot spot. Continuous expansion and shrinkage during bubble clusters or slugs formation and collapsing impose thrusts on the surface, which deteriorates the hydrophilic surface. It can be analogous to cavitation in a pump or turbine propeller where the propeller surface can be damaged by bubble formation or collapsing. On the partial hydrophilic surface, CA increases on an average 15 deg for 1.656 kg/m^2 s, 7 deg for 3.31 kg/m^2 s, and 6 deg for 4.97 kg/m^2 s. For the channel hydrophilic surface, the increment is, on average, 11 deg for 1.656 kg/m^2 s, 2 deg for 3.31 kg/m^2 s, and 4 deg for 4.97 kg/m^2 s. The less degradation on the channel hydrophilic surface is due to the quick removal of bubbles and slugs from the hydrophilic surface. Table 2 represents CA measurement at three different positions, such as upstream, middle, and downstream on the hydrophilic surface of both heat sinks. From these data, it can be

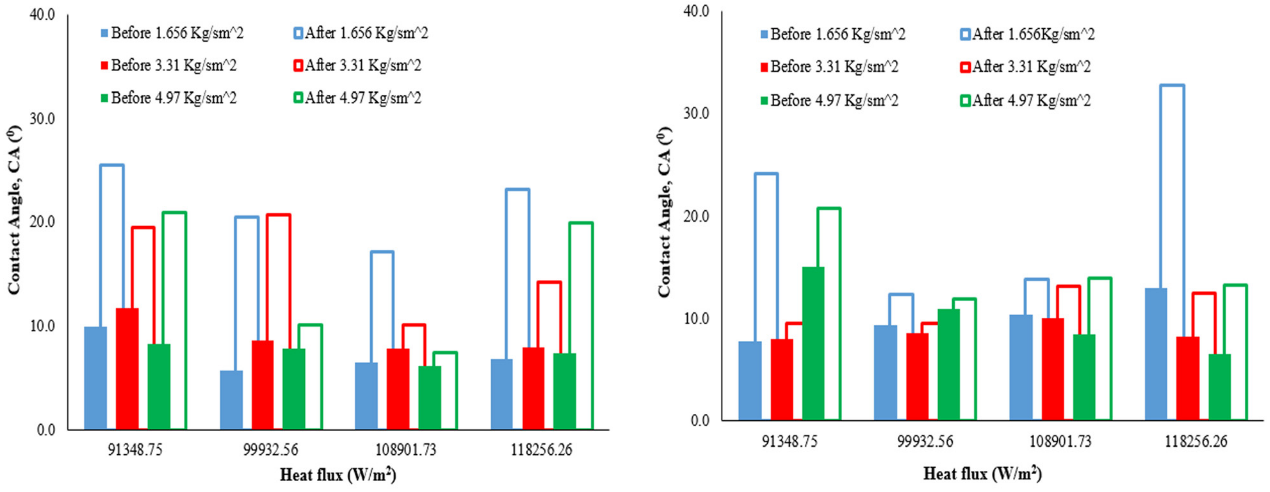

(*a*) (*b*)

Fig. 10 Variation of CA before and after test at different heat fluxes on (*a*) partial hydrophilic and (*b*) channel hydrophilic heat sink

Table 2 Contact angle measurement at three different positions of partial and channel hydrophilic heat sinks for different heat and mass fluxes

		Partial hydrophilic						Channel hydrophilic					
		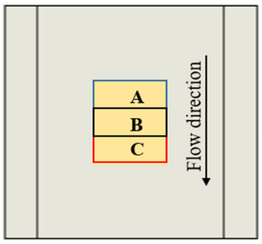						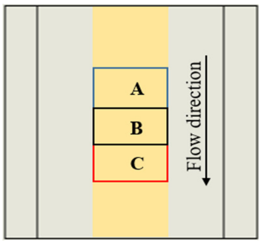					
Mass flux (kg/s m^2)		1.656 kg/s m^2		3.31 kg/s m^2		4.97 kg/s m^2		1.656 kg/s m^2		3.31 kg/s m^2		4.97 kg/s m^2	
Heat flux (W/m^2)	Position	Before	After	Before	After	Before	After	Before	After	Before	After	Before	After
91348.75	*A*	8.3	13.9	13.7	12	8.4	10.6	7.4	24.1	9.4	8	14.5	16.3
	B	9.9	23.6	10.5	12.4	9.1	14.7	6.2	18.7	6.7	9.3	15.3	22.1
	C	11.8	39	11.2	24.4	7.2	37.7	9.8	29.8	7.9	11.2	15.2	23.7
99932.56	*A*	6.2	8.1	9.2	15.5	9.4	9.9	10.1	11.5	8.9	9	9.1	10.2
	B	5.3	20.6	6.3	26.3	7.1	11.5	7.6	9.1	8.2	9.3	12.7	12.1
	C	5.7	32.8	10.5	20.3	6.9	12.2	10.5	16.6	8.7	10.2	11.2	13.4
108901.7	*A*	6.5	9.8	8.6	9.2	7.8	6.4	9.7	12.7	9.8	10.6	9.2	13.6
	B	4.9	12.2	7.2	11	5	7.7	10.2	13.4	10.5	11.7	7.2	10.7
	C	8.1	29.2	7.8	13.3	5.8	8.4	11.3	15.6	9.7	17.3	9	17.7
118256.3	*A*	5.9	17.8	7.7	10.9	9.9	17.3	12.1	21.3	7.3	9.4	7.7	9.9
	B	6.1	26.5	7.4	8.3	6.3	22.3	13.6	42.7	8.8	11.4	5	9.9
	C	8.6	44.3	8.7	23.4	6.1	19.9	13.3	34.1	8.5	16.7	7	15.4

observed that CA increases mainly on the middle and downstream regions where the bubbles generate more frequently and last longer.

4.6 Prediction of Heat Transfer Coefficient Using Artificial Neural Network. To perform the ANN prediction of two-phase heat transfer coefficient, the experimental dataset is divided into training and validation/test sets. Due to the complexity of two-phase flow, the heat transfer coefficient is influenced by various parameters such as temperature, pressure, mass flux, and heat flux. In this study, pertinent parameters such as hot wall temperature, saturated water temperature, differential pressure, mass flux, and heat flux are considered as input to get the predicted value of heat transfer coefficient as output. Among the experiments carried out for different mass fluxes and heat fluxes, 45 input–output pairs are used for conventional, partial hydrophilic, and channel hydrophilic surfaces separately for the ANN prediction. Although 70% of the dataset is allocated randomly as the training set, the remaining 30% of the data is used to validate the network that has been trained using the first set to predict the heat transfer coefficient.

The ANN architecture consists of an input layer, a hidden layer, and an output layer. The accuracy of the prediction depends on the number of hidden layers and their neurons. The optimum number of neurons in the hidden layer relies on the correlation between independent and dependent variables, the number of training, and the set of test data [59]. A fewer number of neurons in the hidden layer is not capable of testing data, hence provides less accuracy. On the contrary, a large number of neurons can lead to overfitting and limit performance [60]. Thus, it is essential to find out the optimal number of neurons in the hidden layer, which can be evaluated by using the trial and error technique. In

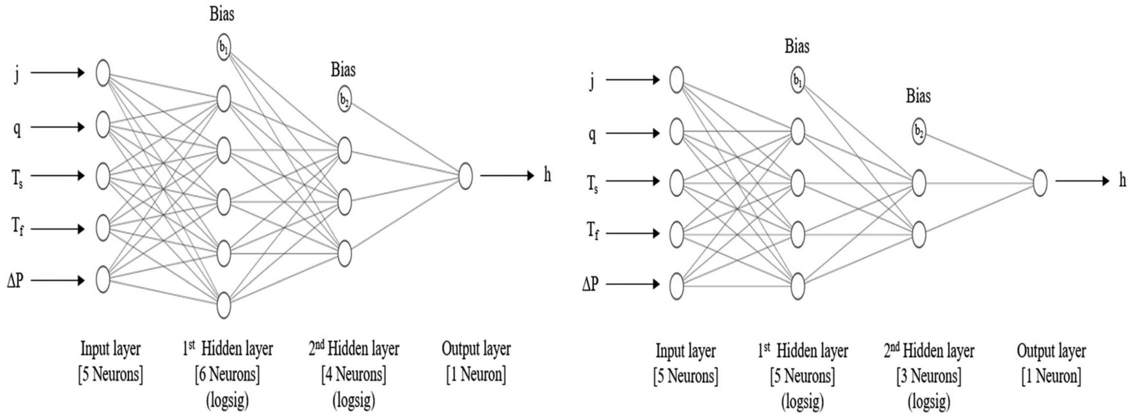

(*a*) (*b*)

Fig. 11 ANN architecture for best performance: (*a*) conventional and channel hydrophilic heat sink and (*b*) partial hydrophilic heat sink

Table 3 Prediction errors for different ANN configurations on conventional, partial hydrophilic, and channel hydrophilic heat sink

Heat sink type	Hidden layers	Neurons in hidden layer	Architecture	MRE (%)	STD$_R$ (%)	Correlation coefficient, R
Conventional	1	9	5-9-1	0.009571419	0.057869138	0.97675
	1	11	5-11-1	0.001263798	0.040357326	0.98883
	1	12	5-12-1	0.004438233	0.020194075	0.9973
	2	5, 3	5-5-3-1	0.004574394	0.019652056	0.9976
	2	6, 3	5-6-3-1	0.00214935	0.011572178	0.99902
	2	**6, 4**	**5-6-4-1**	**0.000822428**	**0.012760201**	**0.99906**
	2	7, 3	5-7-3-1	0.001277549	0.016194706	0.99819
Partial hydrophilic	1	9	5-9-1	0.004570182	0.023680368	0.99506
	1	12	5-12-1	0.003214167	0.030317154	0.99201
	1	13	5-13-1	0.002693888	0.014291533	0.99826
	2	**5, 3**	**5-5-3-1**	**0.000224684**	**0.008662988**	**0.99929**
	2	5, 4	5-5-4-1	0.001164484	0.009090701	0.99923
	2	6, 4	5-6-4-1	0.011725561	0.060544819	0.9638
	2	7, 3	5-7-3-1	0.00403634	0.012658365	0.99842
Channel hydrophilic	1	9	5-9-1	0.003630409	0.027126878	0.99657
	1	10	5-10-1	0.002207216	0.023068065	0.99755
	1	13	5-13-1	0.013178042	0.037604861	0.99329
	2	5, 3	5-5-3-1	0.00123074	0.039666968	0.99287
	2	5, 4	5-5-4-1	0.002634181	0.013075831	0.99919
	2	**6, 4**	**5-6-4-1**	**7.75094×10^{-6}**	**0.009795633**	**0.99955**
	2	7, 4	5-7-4-1	0.002843274	0.01691824	0.99878

Note: Rows in block letter indicate best performance.

this study, the architecture that provides the best performance for conventional, partial hydrophilic, and channel hydrophilic data is shown in Fig. 11. The best performance is considered when the MRE becomes minimum and the correlation coefficient (R) becomes maximum (almost linear).

Different combinations of the hidden layer and its neuron numbers are tested to optimize the ANN performance. As shown in Table 3, for the conventional and channel hydrophilic heat sinks, the minimum MRE and the maximum R are found with two hidden layers having six neurons in the first layer and four neurons in the second layer. For optimal configuration of 5-6-4-1, the MRE and R values are 0.000822428 and 0.99907, respectively, for conventional heat sink and 7.75094×10^{-6} and 0.99955 for channel hydrophilic heat sink. However, the architecture having five neurons in the first layer and three neurons in the second layer provides the best performance for the partial hydrophilic heat sink. The MRE and R values are 0.000224684 and 0.99929, respectively.

Figure 12 illustrates the regression analysis of training, validation, and test data for conventional, partial hydrophilic, and channel hydrophilic heat sinks. The R-value tends to 1, indicating the strong linear correlation between prediction and actual data. This also shows the input parameters, such as temperature, pressure, heat flux, and mass flux, significantly affect the output, heat transfer coefficient. The comparison between the heat transfer coefficient found from the training and prediction (h_{pr}) of optimal ANN model and experimental data (h_{ex}) for conventional, partial hydrophilic, and channel hydrophilic is shown in Fig. 13. The reasonable agreement also indicates that the data fit within ±5% average error, which means a reliable and accurate prediction model.

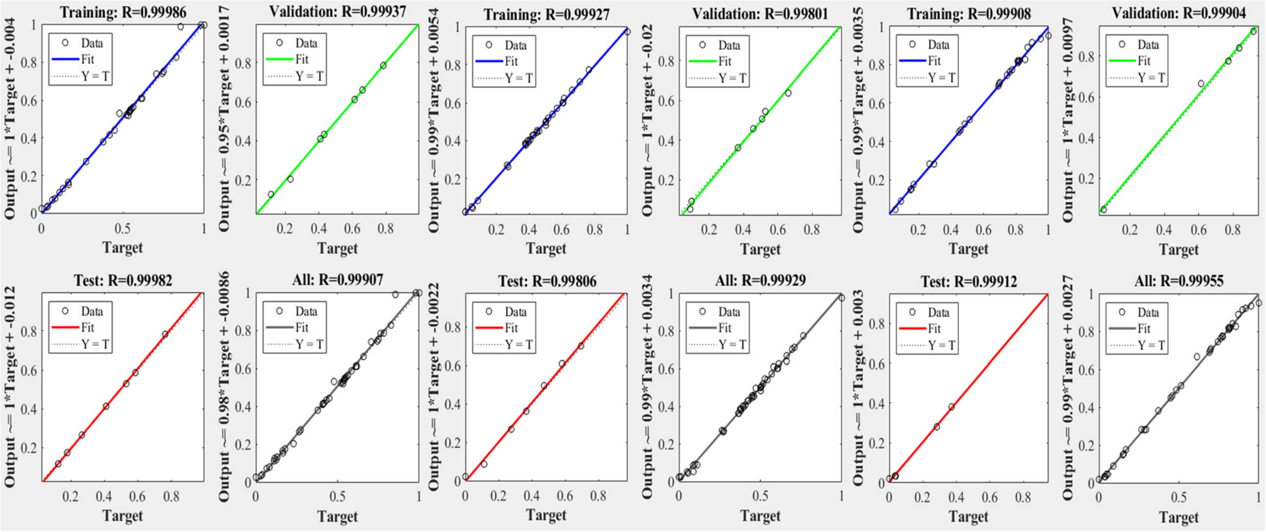

(a) (b) (c)

Fig. 12 Training, validation, and test regression plot for (a) conventional, (b) partial hydrophilic, and (c) channel hydrophilic heat sink

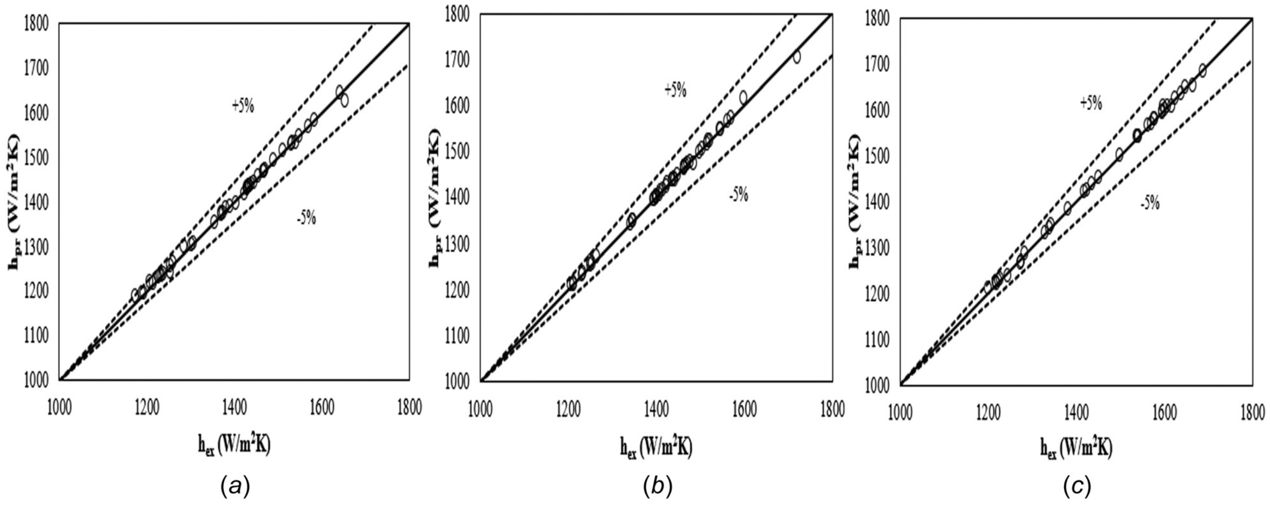

Fig. 13 Comparison of experimental and ANN predicted heat transfer coefficient for best fitting within 5% uncertainty for (*a*) conventional, (*b*) partial hydrophilic, and (*c*) channel hydrophilic heat sink

5 Conclusions

In this study, two different hydrophilic surfaces (partial and channel shape) are fabricated on the microgap heat sink and compared with the conventional (nonhydrophilic) one in terms of the overall flow boiling performance. The experiments are carried out using DI water for a range of heat fluxes varies from 91.35 kW/m^2 to 118.25 kW/m^2 and three different mass fluxes of 1.656 kg/m^2 s, 3.31 kg/m^2 s, and 4.97 kg/m^2 s. Initial vapor film causes short term dry out on the conventional heat sink, which is not found on partial and channel hydrophilic heat sinks due to frequent rewetting and vapor flushing. Among the hydrophilic surfaces, vapor films are flushed more quickly from the channel hydrophilic surface compared to partial hydrophilic. During flow boiling, flow transition occurs from bubbly to slug, and slug flow becomes dominant. These slugs are responsible for increasing the wall temperature and pressure drop. Due to the hydrophilic coating from inlet to outlet on the channel hydrophilic heat sink, water gets a smooth route to pass through the hot spot, which helps to remove more slugs easily. Thus, the channel hydrophilic surface performs better to mitigate hot spot temperature compared to the other two surfaces. The heat transfer coefficient (h) also increases significantly on the channel hydrophilic heat sink at low heat flux ($<$108.9 kW/m^2) except for low mass flux (1.656 kg/m^2 s). However, the heat transfer coefficient goes down on the hydrophilic heat sinks at high heat flux because the saturated entire liquid film remains at the hot spot under the vapor film. The normalized differential pressure decreases with the increase of heat fluxes on the conventional and partial hydrophilic heat sink, but less variation is observed on channel hydrophilic heat sink due to the frequent rewetting. The average contact angle increases more after each test for the partial hydrophilic surface, which indicates the higher degradation of wettability compared to the channel hydrophilic. At low mass flux, 1.656 kg/m^2 s, wettability deteriorates more for both hydrophilic surfaces compared to high mass flux. The ANN prediction of the heat transfer coefficient shows reasonable agreement with experimental data in a band of ±5% average error. The best prediction performance (minimum MRE and maximum R^2) for conventional and channel hydrophilic heat sinks is found for 5-6-4-1 configuration, while for the partial hydrophilic surface, it is 5-5-3-1. Microgap heat sink has the potential of mitigating nonuniform heat fluxes in microscale cooling using flow boiling. The addition of the hydrophilic surface shows the improvement in the cooling performance by frequent rewetting or minimizing dry out time.

Acknowledgment

J.-H. Kim and Y. J. Kim acknowledge the support of the National Science Foundation (CBET-1707056).

Funding Data

- National Science Foundation (CBET-1707056; Funder ID: 10.13039/100000001).

References

[1] Schaller, R. R., 1997, "Moore's Law: Past, Present and Future," IEEE Spectrum, **34**(6), pp. 52–59.
[2] Mudawar, I., 2001, "Assessment of High-Heat-Flux Thermal Management Schemes," IEEE Trans. Compon. Packag. Technol., **24**(2), pp. 122–141.
[3] Bar-Cohen, A., and Wang, P., 2012, "Thermal Management of On-Chip Hot Spot," ASME J. Heat Transfer-Trans. ASME, **134**(5), p. 051017.
[4] Ebadian, M. A., and Lin, C. X., 2011, "A Review of High-Heat-Flux Heat Removal Technologies," ASME J. Heat Transfer-Trans. ASME, **133**(11), p. 110801.
[5] Lee, J., and Mudawar, I., 2009, "Low-Temperature Two-Phase Microchannel Cooling for High-Heat-Flux Thermal Management of Defense Electronics," IEEE Trans. Compon. Packag. Technol., **32**(2), pp. 453–465.
[6] Lee, P.-S., and Garimella, S. V., 2008, "Saturated Flow Boiling Heat Transfer and Pressure Drop in Silicon Microchannel Arrays," Int. J. Heat Mass Transfer, **51**(3–4), pp. 789–806.
[7] Boure, J. A., Bergles, A. E., and Tong, L. S., 1973, "Review of Two-Phase Flow Instability," Nucl. Eng. Des., **25**(2), pp. 165–192.
[8] Tadrist, L., 2007, "Review on Two-Phase Flow Instabilities in Narrow Spaces," Int. J. Heat Fluid Flow, **28**(1), pp. 54–62.
[9] Van Oevelen, T., Weibel, J. A., and Garimella, S. V., 2018, "The Effect of Lateral Thermal Coupling Between Parallel Microchannels on Two-Phase Flow Distribution," Int. J. Heat Mass Transfer, **124**, pp. 769–781.
[10] Dario, E. R., Tadrist, L., and Passos, J. C., 2013, "Review on Two-Phase Flow Distribution in Parallel Channels With Macro and Micro Hydraulic Diameters: Main Results, Analyses, Trends," Appl. Therm. Eng., **59**(1–2), pp. 316–335.
[11] Karayiannis, T. G., and Mahmoud, M. M., 2017, "Flow Boiling in Microchannels: Fundamentals and Applications," Appl. Therm. Eng., **115**, pp. 1372–1397.
[12] Kandlikar, S. G., 2006, "Nucleation Characteristics and Stability Considerations During Flow Boiling in Microchannels," Exp. Therm. Fluid Sci., **30**(5), pp. 441–447.
[13] Kim, S. H., Chu, I. C., Choi, M. H., and Euh, D. J., 2018, "Mechanism Study of Departure of Nucleate Boiling on Forced Convective Channel Flow Boiling," Int. J. Heat Mass Transfer, **126**, pp. 1049–1058.
[14] Qi, S. L., Zhang, P., Wang, R. Z., and Xu, L. X., 2007, "Flow Boiling of Liquid Nitrogen in Micro-Tubes: Part I—The Onset of Nucleate Boiling, Two-Phase Flow Instability and Two-Phase Flow Pressure Drop," Int. J. Heat Mass Transfer, **50**(25–26), pp. 4999–5016.
[15] Hetsroni, G., 1982, *Handbook of Multiphase Systems*, Hemisphere Publishing Corporation, Washington, DC/New York/London.
[16] Peles, Y., 2003, "Two-Phase Boiling Flow in Microchannels: Instabilities Issues and Flow Regime Mapping," ASME Paper No. ICMM2003-1069.
[17] Liu, Y., Fletcher, D. F., and Haynes, B. S., 2013, "On the Importance of Upstream Compressibility in Microchannel Boiling Heat Transfer," Int. J. Heat Mass Transfer, **58**(1–2), pp. 503–512.
[18] Koşar, A., Kuo, C.-J., and Peles, Y., 2006, "Suppression of Boiling Flow Oscillations in Parallel Microchannels by Inlet Restrictors," ASME J. Heat Transfer-Trans. ASME, **128**(3), pp. 251–260.
[19] Kuan, W. K., and Kandlikar, S. G., 2007, "Experimental Study on the Effect of Stabilization on Flow Boiling Heat Transfer in Microchannels," Heat Transfer Eng., **28**(8–9), pp. 746–752.
[20] Lu, C. T., and Pan, C., 2008, "Stabilization of Flow Boiling in Microchannel Heat Sinks With a Diverging Cross-Section Design," J. Micromech. Microeng., **18**(7), p. 075035.

[21] Tamanna, A., and Lee, P. S., 2015, "Flow Boiling Instability Characteristics in Expanding Silicon Microgap Heat Sink," Int. J. Heat Mass Transfer, **89**, pp. 390–405.

[22] Balasubramanian, K., Lee, P. S., Jin, L. W., Chou, S. K., Teo, C. J., and Gao, S., 2011, "Experimental Investigations of Flow Boiling Heat Transfer and Pressure Drop in Straight and Expanding Microchannels—A Comparative Study," Int. J. Therm. Sci., **50**(12), pp. 2413–2421.

[23] Qu, W., 2013, "Two-Phase Cross-Connected Micro-Channel Heat Sink," Patent No. US8479806B2.

[24] Kandlikar, S. G., Kuan, W. K., Willistein, D. A., and Borrelli, J., 2006, "Stabilization of Flow Boiling in Microchannels Using Pressure Drop Elements and Fabricated Nucleation Sites," ASME J. Heat Transfer-Trans. ASME, **128**(4), pp. 389–396.

[25] Koşar, A., Kuo, C.-J., and Peles, Y., 2005, "Boiling Heat Transfer in Rectangular Microchannels With Reentrant Cavities," Int. J. Heat Mass Transfer, **48**(23–24), pp. 4867–4886.

[26] Alam, T., Lee, P. S., Yap, C. R., and Jin, L., 2013, "A Comparative Study of Flow Boiling Heat Transfer and Pressure Drop Characteristics in Microgap and Microchannel Heat Sink and an Evaluation of Microgap Heat Sink for Hotspot Mitigation," Int. J. Heat Mass Transfer, **58**(1–2), pp. 335–347.

[27] Kim, D. W., Rahim, E., Bar-Cohen, A., and Han, B., 2008, "Thermofluid Characteristics of Two-Phase Flow in Micro-Gap Channels," 2008 11th Intersociety Conference on Thermal and Thermomechanical Phenomena in Electronic Systems, Orlando, FL, May 28–31, IEEE, pp. 979–992.

[28] Bar-Cohen, A., and Rahim, E., 2007, "Modeling and Prediction of Two-Phase Refrigerant Flow Regimes and Heat Transfer Characteristics in Microgap Channels," ASME Paper No. ICNMM2007-30216.

[29] Sheehan, J., and Bar-Cohen, A., 2012, "Spatial and Temporal Wall Temperature Fluctuations in Two-Phase Flow in Microgap Coolers," ASME Paper No. IMECE2010-40227.

[30] Alam, T., Lee, P. S., Yap, C. R., and Jin, L., 2012, "Experimental Investigation of Local Flow Boiling Heat Transfer and Pressure Drop Characteristics in Microgap Channel," Int. J. Multiphase Flow, **42**, pp. 164–174.

[31] Nasr, M. H., Green, C. E., Kottke, P. A., Zhang, X., Sarvey, T. E., Joshi, Y. K., Bakir, M. S., and Fedorov, A. G., 2017, "Flow Regimes and Convective Heat Transfer of Refrigerant Flow Boiling in Ultra-Small Clearance Microgaps," Int. J. Heat Mass Transfer, **108**, pp. 1702–1713.

[32] Han, X., Fedorov, A., and Joshi, Y., 2016, "Flow Boiling in Microgaps for Thermal Management of High Heat Flux Microsystems," ASME J. Electron. Packag., **138**(4), p. 040801.

[33] Yang, Y., and Fujita, Y., 2004, "Flow Boiling Heat Transfer and Flow Pattern in Rectangular Channel of Mini-Gap," ASME Paper No. ICMM2004-2383.

[34] Bogojevic, D., Sefiane, K., Walton, A. J., Lin, H., and Cummins, G., 2009, "Two-Phase Flow Instabilities in a Silicon Microchannels Heat Sink," Int. J. Heat Fluid Flow, **30**(5), pp. 854–867.

[35] Ozdemir, M. R., 2016, "Flow Boiling Heat Transfer in a Rectangular Copper Microchannel," J. Therm. Eng., **2**(3), pp. 761–773.

[36] Trieu Phan, H., Caney, N., Marty, P., Colasson, S., and Gavillet, J., 2011, "Flow Boiling of Water in a Minichannel: The Effects of Surface Wettability on Two-Phase Pressure Drop," Appl. Therm. Eng., **31**(11–12), pp. 1894–1905.

[37] Khanikar, V., Mudawar, I., and Fisher, T., 2009, "Effects of Carbon Nanotube Coating on Flow Boiling in a Micro-Channel," Int. J. Heat Mass Transfer, **52**(15–16), pp. 3805–3817.

[38] Li, D., Wu, G. S., Wang, W., Wang, Y. D., Liu, D., Zhang, D. C., Chen, Y. F., Peterson, G. P., and Yang, R., 2012, "Enhancing Flow Boiling Heat Transfer in Microchannels for Thermal Management With Monolithically-Integrated Silicon Nanowires," Nano Lett., **12**(7), pp. 3385–3390.

[39] Yang, F., Dai, X., Peles, Y., Cheng, P., Khan, J., and Li, C., 2014, "Flow Boiling Phenomena in a Single Annular Flow Regime in Microchannels (II): Reduced Pressure Drop and Enhanced Critical Heat Flux," Int. J. Heat Mass Transfer, **68**, pp. 716–724.

[40] Zhu, Y., Antao, D. S., Chu, K.-H., Chen, S., Hendricks, T. J., Zhang, T., and Wang, E. N., 2016, "Surface Structure Enhanced Microchannel Flow Boiling," ASME J. Heat Transfer-Trans. ASME, **138**(9), p. 091501.

[41] Morshed, A. K. M. M., Paul, T. C., and Khan, J., 2013, "Effect of Cu–Al_2O_3 Nanocomposite Coating on Flow Boiling Performance of a Microchannel," Appl. Therm. Eng., **51**(1–2), pp. 1135–1143.

[42] Choi, C., Shin, J. S., Yu, D. I., and Kim, M. H., 2011, "Flow Boiling Behaviors in Hydrophilic and Hydrophobic Microchannels," Exp. Therm. Fluid Sci., **35**(5), pp. 816–824.

[43] Liu, T. Y., Li, P. L., Liu, C. W., and Gau, C., 2011, "Boiling Flow Characteristics in Microchannels With Very Hydrophobic Surface to Super-Hydrophilic Surface," Int. J. Heat Mass Transfer, **54**(1–3), pp. 126–134.

[44] Trieu Phan, H., Caney, N., Marty, P., Colasson, S., and Gavillet, J., 2012, "Flow Boiling of Water on Nanocoated Surfaces in a Microchannel," ASME J. Heat Transfer-Trans. ASME, **134**(2), p. 020901.

[45] Wang, B., He, M., Wang, H., and Qiu, H., 2017, "Flow Boiling Heat Transfer in Wettability Patterned Microchannels," 2017 16th IEEE Intersociety Conference on Thermal and Thermomechanical Phenomena in Electronic Systems (ITherm), Orlando, FL, May 30–June 2, pp. 759–766.

[46] Lewis, J. M., and Wang, Y., 2019, "Two-Phase Frictional Pressure Drop in a Thin Mixed-Wettability Microchannel," Int. J. Heat Mass Transfer, **128**, pp. 649–667.

[47] Jo, H., Park, H. S., and Kim, M. H., 2016, "Single Bubble Dynamics on Hydrophobic–Hydrophilic Mixed Surfaces," Int. J. Heat Mass Transfer, **93**, pp. 554–565.

[48] Thibault, J., and Grandjean, B. P. A., 1991, "A Neural Network Methodology for Heat Transfer Data Analysis," Int. J. Heat Mass Transfer, **34**(8), pp. 2063–2070.

[49] Jambunathan, K., Hartle, S. L., Ashforth-Frost, S., and Fontama, V. N., 1996, "Evaluating Convective Heat Transfer Coefficients Using Neural Networks," Int. J. Heat Mass Transfer, **39**(11), pp. 2329–2332.

[50] Romero-Méndez, R., Lara-Vázquez, P., Oviedo-Tolentino, F., Durán-García, H. M., Pérez-Gutiérrez, F. G., and Pacheco-Vega, A., 2016, "Use of Artificial Neural Networks for Prediction of the Convective Heat Transfer Coefficient in Evaporative Mini-Tubes," Ing. Invest. Tecnol., **17**(1), pp. 23–34.

[51] Kumar, M. K. H., Vishweshwara, P. S., and Gnanasekaran, N., 2020, "Evaluation of Artificial Neural Network in Data Reduction for a Natural Convection Conjugate Heat Transfer Problem in an Inverse Approach: Experiments Combined With CFD Solutions," Sādhanā, **45**(1), p. 78.

[52] Rabbi, K. M., Sheikholeslami, M., Karim, A., Shafee, A., Li, Z., and Tlili, I., 2020, "Prediction of MHD Flow and Entropy Generation by Artificial Neural Network in Square Cavity With Heater-Sink for Nanomaterial," Phys. A: Stat. Mech. Appl., **541**, p. 123520.

[53] Scalabrin, G., Condosta, M., and Marchi, P., 2006, "Flow Boiling of Pure Fluids: Local Heat Transfer and Flow Pattern Modeling Through Artificial Neural Networks," Int. J. Therm. Sci., **45**(8), pp. 739–751.

[54] Scalabrin, G., Condosta, M., and Marchi, P., 2006, "Modeling Flow Boiling Heat Transfer of Pure Fluids Through Artificial Neural Networks," Int. J. Therm. Sci., **45**(7), pp. 643–663.

[55] Alimoradi, H., and Shams, M., 2017, "Optimization of Subcooled Flow Boiling in a Vertical Pipe by Using Artificial Neural Network and Multi Objective Genetic Algorithm," Appl. Therm. Eng., **111**, pp. 1039–1051.

[56] Ertunc, H. M., 2006, "Prediction of the Pool Boiling Critical Heat Flux Using Artificial Neural Network," IEEE Trans. Compon. Packag. Technol., **29**(4), pp. 770–777.

[57] Balcilar, M., Dalkilic, A. S., Suriyawong, A., Yiamsawas, T., and Wongwises, S., 2012, "Investigation of Pool Boiling of Nanofluids Using Artificial Neural Networks and Correlation Development Techniques," Int. Commun. Heat Mass Transfer, **39**(3), pp. 424–431.

[58] Shirley, R., Chakrabarti, D. P., and Das, G., 2012, "Artificial Neural Networks in Liquid-Liquid Two-Phase Flow," Chem. Eng. Commun., **199**(12), pp. 1520–1542.

[59] Naphon, P., Wiriyasart, S., Arisariyawong, T., and Nakharintr, L., 2019, "ANN, Numerical and Experimental Analysis on the Jet Impingement Nanofluids Flow and Heat Transfer Characteristics in the Micro-Channel Heat Sink," Int. J. Heat Mass Transfer, **131**, pp. 329–340.

[60] Qiu, Y., Garg, D., Zhou, L., Kharangate, C. R., Kim, S.-M., and Mudawar, I., 2020, "An Artificial Neural Network Model to Predict Mini/Micro-Channels Saturated Flow Boiling Heat Transfer Coefficient Based on Universal Consolidated Data," Int. J. Heat Mass Transfer, **149**, p. 119211.

[61] Hong, S., Dang, C., and Hihara, E., 2019, "Experimental Investigation on Flow Boiling in Radial Expanding Minichannel Heat Sinks Applied for Low Flow Inertia Condition," Int. J. Heat Mass Transfer, **143**, p. 118588.

[62] McCulloch, W. S., and Pitts, W., 1943, "A Logical Calculus of the Ideas Immanent in Nervous Activity," Bull. Math. Biophys., **5**(4), pp. 115–133.

[63] Kalogirou, S. A., 2001, "Artificial Neural Networks in Renewable Energy Systems Applications: A Review," Renewable Sustainable Energy Rev., **5**(4), pp. 373–401.

[64] Islam, M. R., Sablani, S. S., and Mujumdar, A. S., 2003, "An Artificial Neural Network Model for Prediction of Drying Rates," Drying Technol., **21**(9), pp. 1867–1884.

[65] Karim, A., and Kim, J.-H., 2020, "Study of Two-Dimensional Flow-Boiling Morphological Characteristics in the Micro Gap With Surface Wettability on Hot Spot," ASME Paper No. IMECE2019-11015.